

Adaptive Implicit Finite Element Methods for Multicomponent Compressible Flow in Heterogeneous and Fractured Porous Media

Joachim Moortgat¹

¹School of Earth Sciences, The Ohio State University, Columbus, Ohio, USA.

Key Points:

- Three orders of magnitude gains in efficiency are achieved for fractured domains
- Numerical dispersion is reduced as compared to fully implicit methods
- Robustness, accuracy, and efficiency is demonstrated for hydrogeological and energy applications

Abstract

This work presents adaptive implicit first- and second-order discontinuous Galerkin (DG) methods for the transport of multicomponent compressible fluids in heterogeneous and fractured porous media, discretized by triangular, quadrilateral, and hexahedral grids. The *adaptive* implicit method (AIM) combines the advantages of purely explicit or implicit methods (in time). In grid cells with high fluxes or low pore volumes, the transport update is done implicitly to alleviate the Courant-Friedrichs-Lewy (CFL) time-step constraints of the conditionally-stable explicit approach. Grid cells with a large CFL condition are updated explicitly. Combined, this allows higher efficiency than explicit methods, but it reduces the ‘penalty’ of implicit methods, which exhibit high numerical dispersion and are more computationally and storage expensive *per* time-step. The advantages of AIM are modest for uniform grids and rock properties. However, in heterogeneous or fractured reservoirs explicit methods may become impractical, while a fully implicit approach introduces unnecessary numerical dispersion and is overkill for low permeability layers and matrix blocks. In such applications, AIM is shown to be significantly more efficient and accurate. The division between explicit and implicit grid cells is made adaptively in space and time. This allows for a high level of explicitness and can also adapt to high fluxes caused by, e.g., viscous and gravitational flow instabilities. Numerical examples demonstrate the powerful features of AIM to model, e.g., solute transport, carbon sequestration in saline aquifers, and miscible gas injection in fractured oil and gas reservoirs.

1 Introduction

The transport of multiple species through subsurface porous media is prevalent in hydrogeology and hydrocarbon reservoirs. In hydrogeology, we often want to predict the spreading of dissolved contaminants, whether human induced (e.g., radionuclides, nitrates, hydrocarbons, and various chemicals) or naturally occurring (e.g., arsenic, barium, beryllium, salts). This process can be modeled as multiple solutes in a weakly compressible aqueous phase. The solute concentrations are generally low and the aqueous phase density and viscosity only weakly depend on changing compositions. The sequestration of anthropogenic carbon dioxide (CO₂) in saline aquifers is another hydrogeology application in which we aim to predict the solution trapping of dissolved CO₂ in a multicomponent brine (which can consist of H₂O, salts, noble gases, and migrating light hydrocarbons).

An important energy-related multicomponent single-phase transport problem is enhanced oil recovery (EOR) by miscible gas injection. Gas, such as CO₂, is injected in a reservoir to displace oil (or gas) and when the reservoir is above the minimum miscibility pressure, injected gas will dissolve at all proportions. This process is referred to as first-contact-miscible (FCM) displacement and is efficient because single-phase flow does not suffer from the residual saturations, relative permeabilities, and capillary effects that negatively affect multiphase flow. Dissolution of CO₂ in oil also tends to exhibit favorable phase behavior, such as volume swelling and a viscosity reduction, which aid hydrocarbon recovery. For these reasons, CO₂ injection is a promising EOR strategy and has been used in numerous reservoirs throughout the United States and worldwide. In EOR applications, the molar fractions of all species i (z_i of, e.g., CO₂, nitrogen, and multiple hydrocarbons) can cover the full range $0 < z_i < 1$, viscosities and densities depend non-linearly on compositions, and fluid compressibility cannot be neglected. A rigorous representation of fluid properties requires an equation-of-state (EOS).

Direct observations of *in-situ* flow through porous media are extremely limited and predictions for contaminant transport, CO₂ storage in saline aquifers, and hydrocarbon production efficiencies rely largely on numerical reservoir simulations. Many reservoir simulators have been developed in the past decades in industry (e.g., the Computer Modeling Group’s GEM, Schlumberger’s Eclipse, Landmark’s Nexus, and oil companies’ in-house simulators), national laboratories (e.g., STOMP/STORM, [Bacon *et al.*, 2004; White

et al., 2012], TOUGH [Pruess, 2004], FEHM [Zyvoloski, 2007], PFLOTRAN [Lichtner *et al.*, 2013]), and academia (e.g., UTOUGH [Chang, 1990], IPARS [Wheeler and Wheeler, 1990], MRST [Krogstad *et al.*, 2015; Lie *et al.*, 2012], GPRS [Abushaikh *et al.*, 2009], and many others).

All reservoir simulators solve the main governing equations of flow and transport in porous media: Darcy's law for phase fluxes, a pressure relation, and the conservation of mass. Additional relations can be added for non-isothermal flow, chemical reactions, and other processes which will not be considered in this work. Pressures (and derived fluxes) are almost always obtained by implicit methods in time. When the transport equations are also solved implicitly, we have either fully coupled methods (IMP) or sequential implicit methods (IMPIC, for implicit-pressure-implicit-composition). Implicit methods have become the preferred choice in industry. They are unconditionally stable, allowing for large time-steps, and are thus efficient, especially for black oil simulations that involve a small number of unknowns. However, greater stability does not imply greater accuracy, and implicit methods are known to exhibit greater numerical dispersion than explicit methods on the same grid [Young and Russell, 1993]. In addition, the simultaneous global solution of all independent variables in implicit methods requires much higher computational and memory resources *per time-step* than an explicit update, especially when the number of coupled unknowns increases. For these reasons, implicit-pressure-explicit-composition (IMPEC) schemes are a popular choice for multicomponent multiphase flow simulations. For relatively uniform grids and rock properties, IMPEC methods for multicomponent flow are often more efficient and accurate than IMP or IMPIC.

The explicit transport update in the IMPEC schemes is *conditionally* stable, though, and involves a constraint on the maximum stable time-step. This CFL [Courant *et al.*, 1928] constraint is proportional to a grid-cell's pore volume and inversely proportional to fluxes [Coats, 2003]. In traditional IMPEC implementations, a single time-step for the entire reservoir is determined by the smallest CFL condition in the grid. This means that without special considerations, a few grid cells with a small volume (e.g., pinch-outs in a poor quality grid) or with low porosities can result in small time-steps for the entire simulations [Forsyth *et al.*, 1986]. Similarly, the coning of fluids around wells and channeling through high permeability layers and fractures means that fluid fluxes can be orders of magnitude higher in such preferential pathways than in tighter layers and rock matrices elsewhere in the formation. When one plots the CFL-condition for each grid cell, it is clear that stable time-steps are 1–4 orders of magnitude smaller near wells and in fractures than in the rest of the domain. IMPEC methods may update the transport equations in the bulk of the domain much more often than necessary, while implicit methods are unnecessary expensive (and dispersive) for those grid cells. It is intuitively clear that the best approach would be to combine the benefits of each method while avoiding its limitations. This is the objective of *adaptive* implicit methods (AIM).

AIM is not a new concept and was first proposed in the 1980's by Thomas *et al.* [1982]; Thomas and Thurnau [1983], compared to IMP methods by Forsyth and Sammon [1986]; Collins *et al.* [1992] and to the IMPEC approach by Young and Russell [1993]. These works, as well as Watts and Rame [1999]; Grabenstetter *et al.* [1991]; Fung *et al.* [1989]; Tan *et al.* [1988], also investigated different switching logics between implicit and explicit grid cells, moving from early heuristic choices based on changes in variables to more quantitative criteria, e.g., based on a CFL condition [Russell *et al.*, 1989] or other stability criteria (e.g., Fung *et al.* [1989]). Stability criteria for a *thermal* AIM method were derived by Moncorgé and Tchelepi [2009]; Maes *et al.* [2013]. More recently, algebraic multi-grid solvers were developed for AIM [Clees *et al.*, 2010], AIM was tested in a parallel industry reservoir simulator [Lu *et al.*, 2009], and an AIM version of the implicit-pressure-implicit-saturation (IMPSAT) scheme was developed [Cao and Aziz, 2002; Zhou *et al.*, 2011].

The aforementioned efforts have demonstrated the feasibility and robustness (when appropriate switching logic is used) of AIM methods, but found only relatively modest improvements in computational efficiency, ranging from no improvement [Young and Russell, 1993] to a factor 2–3 [Collins *et al.*, 1992], rather than by orders of magnitude. Perhaps because of these findings, AIM methods seem to have attracted less interest in the past decade. However, the reason for the small observed performance gains may be that numerical test cases have considered relatively uniform grids and relatively homogeneous unfractured reservoirs.

In fractured or highly heterogeneous reservoirs, the advective flow rates through fractures or high permeability (e.g., sandstone) layers may be many orders of magnitude higher than through the rock matrix or tight shale layers. CFL conditions in the former regions can easily be three orders of magnitude smaller than for the latter, which makes IMPEC schemes highly inefficient. Fractured reservoirs, in which *discrete* fractures are represented, are the prime application for AIM simulations.

The basic idea has been applied by Hoteit and Firoozabadi [2008a]; Zidane and Firoozabadi [2014], who used a second-order finite element IMPEC scheme for the rock matrix, and a first-order IMPIC scheme for fractures that were represented by a grid of $(D - 1)$ -dimensional elements (with $D = 2$ for two-dimensional and $D = 3$ for three-dimensional simulations). The division between explicit matrix grid cells and implicit fracture grid cells is determined *a priori* in this approach, whether or not significant fluid flow occurs through a given fracture. Such a static division of explicit and implicit grids could also be generalized to well regions and heterogeneous permeabilities.

This work proposes a truly adaptive implicit method for discretely fractured reservoirs and uses the same order accuracy in both matrix and fractured elements. A simple switching logic is shown to be adequate to define which grid cells need to be updated implicitly and which can be done explicitly, at each time-step and each spatial location. This approach can be applied, without special treatment, to naturally fractured reservoirs, highly heterogeneous (e.g., layered) formations, well regions, and even to the heterogeneous flow patterns that occur, even in homogeneous media, due to viscous and gravitational flow instabilities (fingering).

AIMs are presented to update the transport equations for multicomponent compressible fluids discretized by both element-wise-constant finite volume (FV) and multilinear discontinuous Galerkin (DG) methods on triangular, quadrilateral, and hexahedral grids. Pressures and fluxes are computed simultaneously by the implicit mixed-hybrid-finite-element (MHFE) method [Chavent and Roberts, 1991; Chavent and Jaffre, 1986]. Additional constraints can be imposed on the tangential fluxes across material interfaces [Zhou *et al.*, 2001; Cainelli *et al.*, 2012]. Discrete fractures are modeled by the cross-flow-equilibrium (CFE) approach [Hoteit and Firoozabadi, 2005]. In this approach, fractures are represented by D -dimensional CFE elements that include both the tiny fractures (with an aperture of ≤ 1 mm) and a small slice of the matrix on either side (of the order of centimeters). The FE integrals in the weak form of the governing equations are computed analytically to account for both the fracture and matrix contributions to the CFE fluxes. An attractive feature of the CFE approach is that, once the fluxes throughout the domain are known from the MHFE update, the transport update is identical for matrix and fracture-containing CFE grid cells [Moortgat and Firoozabadi, 2013a,b]. Due to this feature, the AIM methods developed in this work are identical for both fractured and unfractured reservoirs.

Phase behavior is critical in applications such as gas injection in oil reservoirs and CO₂ sequestration in aquifers. To obtain accurate fluid densities and *compressibilities* the [Peng and Robinson, 1976] PR-EOS is used for hydrocarbon fluids, while the cubic-plus-association (CPA) EOS [Li and Firoozabadi, 2009] is used for fluids that contain polar molecules (i.e., brine).

Fickian diffusion and capillary imbibition can be important for gas and water injection, respectively, in fractured oil reservoirs and were considered in earlier work [Moortgat and Firoozabadi, 2013a,c, 2016a]. These processes can be included in a typical operator-splitting approach, and solved implicitly using a mixed formulation such as MHFE [Hoteit and Firoozabadi, 2008b; Hoteit, 2013]. For clarity of presentation, these processes are neglected in this work to focus on the new discretization techniques for advective transport.

In the following, the governing equations and numerical implementation of FV-AIM and DG-AIM methods for multicomponent compressible flow in fractured media are presented first. Then, their robustness, accuracy, and efficiency is demonstrated by six numerical examples of increasing complexity, before concluding with summarizing remarks.

2 Mathematical Framework

We consider a compressible mixture of n_c species, labeled by i , that are advected by a single fiducial Darcy velocity

$$\vec{v} = -\frac{k}{\mu}\nabla(p - \rho g z), \quad (1)$$

with μ the viscosity, p pressure, ρ mass density, g gravitational acceleration, and z the (vertical upwards) height. The tensor k represents both the absolute permeability in the rock matrix k^m and the fracture permeability k^f . The latter is often computed as a (scalar) function of fracture aperture δf .

The mass or molar conservation law is given by

$$\phi \partial_t c_i + \nabla \cdot (c_i \vec{v}) - f_i = 0, \quad \forall i = 1, \dots, n_c, \quad (2)$$

with $c_i = c z_i$ the density of component i , c the total density, and z_i the fraction of species i (with $\sum_i z_i = 1$). Each of these can be defined in a mass or molar reference frame. In the following, the molar frame is chosen, c stands for molar density, ρ for mass density, and the relation between the two is $\rho = \sum_i (c_i w_i)$ in terms of molecular weights w_i . ∂_t is the partial derivative with respect to time t , and f_i represents injection wells.

As discussed in the Introduction, fluid properties depend non-linearly on compositions, temperature T , and pressure. This dependence is most rigorously described by an equation-of-state (EOS). Both the Peng and Robinson [1976] PR-EOS and Li and Firoozabadi [2009] CPA-EOS show a deceptively simple relation between pressure and density:

$$c = \frac{p}{ZRT} + v_s, \quad (3)$$

similar to the ideal gas law with R the universal gas constant. The compressibility factor Z accounts for the non-ideal fluid behavior and hides the complexity of either EOS. In the PR-EOS, Z can be found analytically from a cubic equation. The CPA-EOS involves additional terms to describe association due to polar molecules (such as H₂O or asphaltenes [Nasrabadi et al., 2016]). Z depends on T , p , and z_i , and involves the critical properties and binary interaction coefficients for each species. Solution techniques for this problem are presented in Moortgat et al. [2012]. A volume shift parameter v_s is used to better match experimental densities. Fluid viscosities are also non-linear functions of compositions [Christensen and Pedersen, 2006].

Eqs. (1)–(3) form a closed system of $n_c + 2$ equations for the $n_c + 2$ primary unknowns c_i , p , and \vec{v} . However, the non-linear EOS is difficult to turn into an algebraic solution scheme for the pressure. Therefore, it is more convenient to adopt an explicit pressure equation, which expresses conservation of volumes [Acs et al., 1985; Watts, 1986]:

$$\phi C_f \partial_t p + \sum_{i=1}^{n_c} \bar{v}_i [\nabla \cdot (c_i \vec{v}) - f_i] = 0, \quad (4)$$

and involves the total fluid compressibility C_f and partial molar volumes \bar{v}_i (which depend on compositions through the EOS [Moortgat *et al.*, 2012]). By using Eq. (4), the system of equations is over-specified. To avoid this degeneracy, the volume balance between molar densities from Eqs. (2) and (3) will only be used to check mass balance errors. Neumann conditions are used for impermeable boundaries, except in production wells, which can have either constant rate (Neumann) or constant pressure (Dirichlet) conditions. Initial conditions specify the composition z_i throughout the domain and an initial density and pressure that satisfy hydrostatic equilibrium.

3 Implementation of Adaptive Implicit Methods

3.1 Discrete Fracture Model

The cross-flow-equilibrium (CFE) fracture model represents fractures by D -dimensional elements in the same grid as the matrix. To improve efficiency, as compared to single-continuum models, the computational CFE elements contain both the fracture and a small amount of matrix on both sides. The assumption is that fractures have a high transverse permeability and fluid in the fractures quickly equilibrates with the fluid immediately next to it in the matrix. In other words, instead of explicitly calculating the fracture-matrix flux, the fracture and matrix fluids are instantly mixed. This makes the transport equation easy to implement for fractured domains: once Darcy fluxes are known, the transport equation is *identical* for matrix grid cells and for fracture-containing CFE elements.

It turns out that the CFE numerical solution of the Darcy and pressure equations for fractured domains is also quite elegant. Consider a cubic CFE element K with volume $|K| = \Delta x \Delta y \Delta z$, which contains a vertical fracture with aperture δf parallel to the y -axis. The top face E of K has a total surface area of $|E| = \Delta x \Delta y$, while the fracture cross-sectional area is $\delta f \Delta y$. The fraction of $|E|$ intersected by the fracture is $\epsilon_E = \delta f / \Delta x$ while the matrix fraction is $1 - \epsilon$. The weak form of Darcy's law, used in FE methods, involves the normal component of \vec{v} across element faces, denoted as $v_{K,E}$ (and superscripts m and f denote matrix and fracture properties, respectively):

$$v_{K,E} = v_{K,E}^f + v_{K,E}^m = -\frac{k^{\text{eff}}}{\mu} \nabla_E (p - \rho g z). \quad (5)$$

The last expression introduces an *effective* CFE permeability $k^{\text{eff}} = \epsilon_E k^f + (1 - \epsilon_E) k^m$ and relies on the CFE assumption that a CFE element contains a mixed fluid with a single density and viscosity, at a single pressure. In terms of k^{eff} , the FE solution of Darcy velocities is also identical to that for unfractured domains. On general unstructured grids, ϵ_E can be more complicated, but ϵ_E , as well as the effective porosities of CFE elements, only need to be taken care of in an initialization step. Moortgat and Firoozabadi [2013b,a] present the details of the *implicit* MHFE method that simultaneously solves for continuous pressures and velocities throughout the fractured domain.

The common approach is adopted of decoupling the flow from the transport. When Eq. (2) is solved by an explicit method, such as forward Euler, this results in the IMPEC scheme. When an implicit method, like backward Euler, is used, the scheme is referred to as implicit-pressure-implicit-composition, or IMPIC [Moortgat *et al.*, 2016]. The purpose of this work is to combine the benefits of IMPEC and IMPIC in an *adaptive* implicit method, or AIM. All three approaches use the same MHFE update. The remainder will thus only concern the solution to the transport equation, Eq. (2).

As a final note, it is acknowledged that the instant equilibration within a CFE element is an approximation. In our prior work on CFE fractured reservoir modeling, we relied on an IMPEC scheme. Therefore, relatively wide CFE elements were sometimes required to maintain reasonable CFL time-step sizes. When fractures are modeled implicitly, though, there is no such restriction on the CFE width, and the CFE elements could

theoretically be chosen as narrow as the fracture aperture. *Zidane and Firoozabadi* [2014] demonstrated that for such grids the CFE and a $(D - 1)$ implicit FV fracture model agree remarkably well. The CFE approach has been validated against other simulators and with experimental data in previous work (e.g., *Moortgat and Firoozabadi* [2013a,b,c, 2016a]).

3.2 Transport Updates

A useful property of single-phase multicomponent flow is that, in decoupled IM-PEC and IMPIC schemes, Eq. (2) is *linear* in the molar densities of each species, c_i . This means that the equation can be solved for each species *individually*, which results in an extremely efficient numerical scheme. The subscript i will be dropped from here on.

3.2.1 First-order IMPEC and IMPIC schemes

The lowest-order discontinuous Galerkin (DG) discretization of the molar conservation Eq. (2) is equivalent to a single-point upweighted finite volume (FV) scheme. The update of Eq. (2) from time-step n to time $n + 1$ of a grid cell K (with neighbors K'), using an implicit backward Euler (with $m = n + 1$) or explicit forward Euler ($m = n$), can be written as

$$c_K^{n+1} = c_K^n - \delta\tau_K \left(\sum_{E \in \partial K} \tilde{c}_{K,E}^m v_{K,E} - F_K^m \right) \begin{cases} \tilde{c}_{K,E} = c_K & \forall q_{K,E} \geq 0 \\ \tilde{c}_{K,E} = c_{K'} & \forall q_{K,E} < 0 \\ E = K \cap K' \end{cases} \quad (6)$$

where $\delta\tau_K = \Delta t / (\phi_K |K|)$ and $\tilde{c}_{K,E}$ is the upwind choice that defines a continuous flux across faces E . $F_{i,K} = |K| f_{i,K}$ is the number of moles of species i injected in K per second. Eq. (6) can be written in matrix form as

$$\mathbf{c}^{n+1} = \mathbf{A}_- \mathbf{c}^n + \mathbf{f} \quad , \quad \text{explicit FV} \quad (7)$$

$$\mathbf{A}_+ \mathbf{c}^{n+1} = \mathbf{c}^n + \mathbf{f} \quad , \quad \text{implicit FV} \quad (8)$$

$$\mathbf{A}_\pm = (\mathbf{I} \pm \mathbf{dt}\mathbf{Q}) \quad , \quad (9)$$

where \mathbf{c} , and \mathbf{f} are vectors of length N_K , the number of grid cells, \mathbf{I} is the $N_K \times N_K$ identity matrix, \mathbf{dt} is an equal size diagonal matrix with elements $[\mathbf{dt}]_{K,K} = \delta\tau_K$, and $[\mathbf{f}]_K = f_K \delta\tau_K$. The matrix \mathbf{Q} determines the upwind molar densities for a given velocity field. Its components are discussed in *Aarnes et al.* [2007].

The basic sparsity pattern for a triangular, a quadrilateral, and a hexahedral grid are shown in Figure 1. Because upwind directions depend on the velocity field, the sparsity pattern (the non-zero elements of \mathbf{Q} , and thus \mathbf{A}_\pm) depends on well placements and evolves in time. This is shown in Figure 1 for injection from either the bottom or the top of a quarter-five-spot injector-producer configuration. Note that many of the examples in this work are for structured Cartesian 2D or 3D grids. The FE methods, however, are implemented for any unstructured triangular, quadrilateral, or hexahedral grid and use typical FE element numbering from $1, \dots, N_K$, rather than Cartesian-type indexing. This flexibility of (re)numbering elements in FE methods is critical in the development of AIM schemes in the next section.

3.2.2 First-order AIM scheme

Let us reiterate the motivation to develop *adaptive* implicit schemes for Eqs. (7) and (8). Eqn. (7), for IMPEC, only involves a direct multiplication of a sparse matrix with the N_K -length vector of known molar densities from the previous time-step. This operation is cheap, but it has to be performed many times because IMPEC has a maximum Δt . Conversely, the implicit transport update Eqn. (8) is unconditionally stable for any (larger) Δt , but each update involves *inverting* the sparse matrix \mathbf{A}_+ , which is a more computationally expensive operation, especially for large matrices (e.g. in 3D). In addition, the implicit

update may be more stable, but is less accurate [Young and Russell, 1993]. So the objective is to *split* the grid into separate explicit and implicit elements and to update as many elements as possible explicitly, with the faster Eqn. (7), while achieving a bigger stable time-steps by using Eqn. (8) for the elements with the strictest CFL constraints.

Figure 2 illustrates the key concept. Fluid is injected from 1 element in the bottom-left corner and produced from 1 element in the top-right corner of a 10×10 quadrilateral horizontal grid (three contours of composition are shown at 40% pore-volume injected, or PVI). All elements have the same size, permeability, and porosity. A basic mass-conservation argument suggests that in this configuration, the flux through edges in the middle of the domain is $\approx \sqrt{N_K}$ smaller than the fluxes in well grid cells. Because all grid cells have the same pore volume, this implies that the local CFL condition is $\approx \sqrt{N_K} = 10$ higher in the middle than near the wells. Figure 2 has labels in each grid cell for ϑ_K , which is the local CFL condition (Δt_K) in element K divided by its smallest value anywhere in the domain (Δt_{CFL}). It shows that indeed $\vartheta = 1$ in wells and $7 < \vartheta_K < 30$ furthest away from wells.

Now assume that the grid Ω with $N_K = 10 \times 10$ can be split into an implicit sub-grid Ω^{imp} with $N_K^{\text{imp}} = 38$ elements and an explicit grid Ω^{exp} with $N_K^{\text{exp}} = 62$ elements (the switching logic is discussed below). As mentioned above, FE methods allow for unstructured grids, and the explicit and implicit sub-grids in Figure 2 can be updated with Eqs. (7) and (8), respectively, by simply renumbering the grid cells within each subgrid. The interface, Γ^{bc} , between the two grids is treated as a boundary condition, which has 20 edges E^{bc} in this example. More specifically, first the explicit update of Ω^{exp} is carried out with Γ^{bc} treated as an open boundary (at a given Neumann flux condition). For the subsequent implicit update, the total number of moles (of each species) that crossed each $E^{\text{bc}} \in \Gamma^{\text{bc}}$ in the explicit update, is added as a source or sink term \mathbf{f}^{bc} to the implicit update on grid Ω^{imp} , and with a no-flow Neumann condition on Γ^{bc} . Together, these boundary conditions guarantee conservation of moles.

The interface term \mathbf{f}^{bc} could be computed from Eqn. (7) for Ω by setting $v_{K,E} = 0$, $\forall E \ni \Gamma^{\text{bc}}$ in $\mathbf{Q} = \mathbf{Q}^{\text{bc}}$:

$$\mathbf{f}^{\text{bc}} = \mathbf{c}^{n+1} - \mathbf{c}^n = \mathbf{A}_- \mathbf{c}^n - \mathbf{c}^n = -\mathbf{dt} \mathbf{Q}^{\text{bc}} \mathbf{c}^n. \quad (10)$$

Next, the elements in the implicit grid Ω^{imp} are renumbered to $1, \dots, N_K^{\text{imp}}$, and \mathbf{f}^{bc} becomes a N_K^{imp} -length vector with only the elements on Γ^{bc} non-zero. Adding these ‘wells’ to Eqn. (8), one has

$$\mathbf{A}_+ \mathbf{c}^{n+1} - \mathbf{f} = \mathbf{c}^n + \mathbf{f}^{\text{bc}} = (\mathbf{I} - \mathbf{dt} \mathbf{Q}^{\text{bc}}) \mathbf{c}^n = \mathbf{A}_-^{\text{bc}} \mathbf{c}^n, \quad \forall K \in \Omega^{\text{imp}}. \quad (11)$$

But the right-hand-side is of course exactly the contribution of explicit fluxes across Γ^{bc} to boundary elements. This suggests a more straightforward solution method. First, Eqn. (7) is done for all Ω , but now with $\mathbf{Q} = \mathbf{Q}^{\text{expl}}$ (and similarly $\mathbf{A}_-^{\text{expl}}$) defined by $v_{K,E} = 0$, $\forall E = K \cap K'$ with $K, K' \in \Omega^{\text{imp}}$:

$$\mathbf{c}^k = \mathbf{A}_-^{\text{expl}} \mathbf{c}^n, \quad \forall K \in \Omega = \Omega^{\text{exp}} \cup \Omega^{\text{imp}}. \quad (12)$$

For all elements in Ω^{exp} , $\mathbf{c}^k = \mathbf{c}^{n+1}$. For all elements in Ω^{imp} that are not on Γ^{bc} , $\mathbf{c}^k = \mathbf{c}^n$, and finally, for the elements in Ω^{imp} on Γ^{bc} , $\mathbf{c}^k = \mathbf{c}^n + \mathbf{f}^{\text{bc}}$, e.g., updated with the sources and sinks from the explicit update across Γ^{bc} .

The implicit update can now be written as

$$\mathbf{A}_+ \mathbf{c}^{n+1} = \mathbf{c}^k + \mathbf{f}, \quad \forall K \in \Omega^{\text{imp}}. \quad (13)$$

As an example, for the $N_K = 100$ element grid in Figure 2, one could choose to only update the 1 injection well and 1 production well implicitly, while using IMPEC for the rest of the domain. In that case, Eqn. (12) requires a direct sparse matrix multiplication for the full grid, but the implicit well treatment in the AIM involves the inversion of Eqn. (13) for

only a 2×2 sparse matrix (which also happens to be diagonal in this case, because there is no direct flux between the injection and production grid cells). *Natvig and Lie* [2008]; *Kwok and Tchelep* [2007] propose further optimizations by reordering the grid cells according to flux directions in each element.

Eqs. (12) and (13) define the first-order FV-AIM scheme. What remains is how to decide the level of implicitness, or equivalently, the time-step size.

3.2.3 Switching logic

An implicitness criterion is adopted based on the *adaptive* CFL condition associated with an IMPEC update. At every time-step, the local CFL condition, Δt_K , is computed in each element K and normalized by the smallest Δt_{CFL} to define a dimensionless variable ϑ_K and the level of implicitness is determined by choosing a switching criterion $\vartheta^{\text{switch}}$:

$$\vartheta_K = \left\lfloor \frac{\Delta t_K}{\Delta t_{\text{CFL}}} \right\rfloor \begin{cases} \text{Explicit if } \vartheta_K \geq \vartheta^{\text{switch}} \\ \text{Implicit if } \vartheta_K < \vartheta^{\text{switch}} \end{cases} \quad (14)$$

In other words, the grid is split into subgrid Ω^{imp} defined by $K \in \Omega^{\text{imp}}, \forall K$ with $\vartheta_K < \vartheta^{\text{switch}}$, and grid $\Omega^{\text{expl}}, \forall K$ with $\vartheta_K \geq \vartheta^{\text{switch}}$. To add another level of robustness, e.g., to avoid isolated grid cells that fall just below the switching criterion, a simple smoothing algorithm is used in which any explicit grid cell that has an implicit neighbor is also updated implicitly, both in the first pass and in a second pass through all elements. Figure 2 illustrates the switching logic for $\vartheta^{\text{switch}} = 4$.

For this simple example on a coarse grid, fluxes and associated CFL conditions are relatively uniform and 38% – 44% of elements have to be solved implicitly. For more realistic 3D examples, especially for heterogeneous and fractured formations, the range of CFL conditions can vary by several orders of magnitude. Often only a small percentage of elements have to be solved implicitly to achieve high gains in $\vartheta^{\text{switch}}$ (as demonstrated in the Numerical Experiments for $\vartheta^{\text{switch}}$ up to 1,500). Eqs. (12) and (13), together with this switching criterion, prove to be numerically stable for a wide range of challenging test cases. The same criterion is used for the DG-AIM schemes discussed next.

3.2.4 Second-order DG IMPEC, IMPIC, and AIM schemes

To reduce numerical dispersion and achieve high accuracy on coarse grids, a second-order DG transport update is advantageous. Instead of the element-wise-constant fluid properties in FV, the degrees-of-freedom (DOF) are at the element vertices and vary linearly in each spatial dimension within each element. Moreover, variables are allowed to be *discontinuous* across element faces, which is useful, e.g., at fracture-matrix and layer interfaces.

The subscript N is introduced to label the local node number within an element K , and N^{dof} is the number of nodes per element, e.g., 3 for triangles, 4 for quadrilaterals, and 8 for hexahedra. For each node N of element K the molar density $c_{K,N}^{n+1}$ is updated by the DG method as:

$$\sum_{N'=1}^{N^{\text{dof}}} (c_{K,N'}^{n+1} - c_{K,N'}^n) M_{N,N'}^K = -\frac{\Delta t}{\phi_K} \left[\sum_{E \in \partial K} \widetilde{c}_{K,E}^m v_{K,E} M_N^E - \sum_{N'=1}^{N^{\text{dof}}} \sum_{E \in \partial K} c_{K,N'}^m v_{K,E} M_{N,N'}^{K,E} - F_K^m \right], \quad (15)$$

where the matrices $M_{N,N'}^K$, M_N^E , and $M_{N,N'}^{K,E}$ involve integrals of the DG basis functions for c and the MHFE Raviart-Thomas basis vector fields for \vec{v} over the element K and its faces E [*Mikysta and Firoozabadi*, 2010]. Algebraic expressions for Eqn. (15) on triangular, quadrilateral, tetrahedral, prismatic, and hexahedral grids are provided in *Moortgat and*

Firoozabadi [2016b]. As in Eqn. (6), $m = n$ results in an explicit and $m = n + 1$ in an implicit scheme.

The expressions Eqn. (15) for each element K can again be collected in global matrices for the $N^{\text{dof}} \times N_K$ values of c , denoted by the vector \bar{c} :

$$\bar{c}^{n+1} = \bar{\mathbf{A}}_- \bar{c}^n + \mathbf{f} \quad , \quad \text{explicit DG} \quad (16)$$

$$\bar{\mathbf{A}}_+ \bar{c}^{n+1} = \bar{c}^n + \mathbf{f} \quad , \quad \text{implicit DG} \quad (17)$$

All matrices now have dimensions $(N^{\text{dof}} \times N_K)^2$, but \mathbf{I} , \mathbf{dt} , and \mathbf{f}_i have the same value at each node of an element K while $\bar{\mathbf{A}}_{\pm} = (\mathbf{I} \pm \mathbf{dt}\bar{\mathbf{Q}})$.

The two terms on the right-hand-side of Eqn. (15) result from a partial integration of the divergence term in the transport equation. The volume term only involves the N^{dof} nodal values of c inside element K and partially populates a $N^{\text{dof}} \times N^{\text{dof}}$ block around the diagonals of $\bar{\mathbf{A}}_{\pm}$. The surface integral term involves upwind values for $\bar{c}_{K,E}$. Unlike in FV, *multiple* values are upwinded across each face, which communicates not only an average species density, but also its gradient. The upwind dependencies in DG become quite complex, as is illustrated in Figure 3 for a quadrilateral grid. The update of each nodal $c_{K,N}$ can depend on up to 4 nodal values in neighboring elements across the 4 edges (depending flux directions). On triangular and hexahedral grids, each node can depend on nodes in 3 or 6 neighboring elements, respectively. For each *outgoing* flux, $v_{K,E} \geq 0$, the nodal $c_{K,N}$ will be influenced by the local mirror nodes (across edge E) of those illustrated in Figure 3. These complex interdependencies are necessary to maintain a multilinear approximation to c within each element.

Once the matrices $\bar{\mathbf{A}}_{\pm}$ are constructed for the IMPEC and IMPIC updates, given in Eqs. (16)-(17), the AIM scheme is defined exactly the same as for the FV approximation, but DG is stabilized by a slope-limiter [Hoteit and Firoozabadi, 2006]. An example is given in the bottom of Figure 3, which shows DG-AIM simulation results for the same problem as in Figure 2 and with the same switching criterion. The full DG matrices $\bar{\mathbf{A}}_{\pm}$ for this 10×10 grid have 160,000 elements with 1,880 non-zero values. By splitting the grid in 38 implicit and 62 explicit elements, the explicit update involves a direct multiplication of a sparse matrix $\bar{\mathbf{A}}_-$ with 1,432 non-zero elements and the inversion of the implicit matrix $\bar{\mathbf{A}}_+$ with only 640 non-zero elements. As expected, the composition profile shows less numerical dispersion for DG than for the FV results in Figure 1.

4 Numerical Experiments

The six following examples include applications in both hydrocarbon reservoir engineering (Examples 1–3 and 6) and in hydrogeology (Examples 4 and 5). The latter consider the transport of dissolved CO_2 in brine-saturated, highly heterogeneous and fractured, aquifers at an initial pressure of 100 bar and a temperature of $T = 77^\circ \text{C}$. The phase behavior of the CO_2 -water mixtures is modeled by the CPA-EOS. The hydrocarbon examples consider miscible gas (CO_2 and methane) injection in oil and gas reservoirs. The gas reservoir (Example 6) is initially saturated with propane at 50 bar and 124°C conditions. The oil reservoir is saturated with the 5-component fluid in *Moortgat and Firoozabadi* [2013a] (Table 2) at a temperature of $T = 127^\circ \text{C}$ and pressure of 483 bar. At these conditions, the oil is FCM with CO_2 . Both the density of pure CO_2 (686 kg/m^3) and mixtures of CO_2 and oil (e.g., 612 kg/m^3 for 50:50 mol%) are denser than the initial oil in place (571 kg/m^3). At the same time, the viscosities are less (0.05 cp for pure CO_2 , 0.11 cp for a 50:50 mol% mixture, versus 0.18 for the initial oil). Therefore, CO_2 -injection is prone to both viscous and gravitational flow instabilities.

The first three examples are designed to illustrate specific advantages of AIM over fully explicit or implicit methods, while the last three demonstrate the robustness and efficiency of the proposed methods for more realistic and highly challenging applications.

All example simulations are run on a 2.8 GHz Intel Core i7 processor and 16GB RAM. The off-the-shelf Pardiso linear solver is used for both the MHFE global pressure and the IMPIC and AIM FV and DG transport updates.

4.1 Stable displacement in a quarter-five-spot uniform domain

As a first illustrative example, the classical quarter-five-spot set-up is modeled with one injection well and one diagonally opposite production well. The domain is 1 km by 1 km horizontally (in 2D) and 100 m in the vertical direction (in 3D), discretized by a uniform quadrilateral (2D) or hexahedral (3D) grid with grid sizes of 10 m in each direction. The domain has a uniform permeability of 10 md and porosity of 20%. Injection is at a constant rate of 5% pore volume (PV) per year from a perforated vertical well at the origin, and production is at a constant pressure from the opposite corner. To compare 2D and 3D simulations, gravity is neglected in this example.

The purpose of this example is to compare CPU times and accuracy for different numerical methods. But CO_2 injection is viscously unstable and simulations with different levels of numerical dispersion show varying degrees of fingering, which makes the results hard to compare. To make a more straightforward comparison between the methods, a stable displacement process is simulated by injecting the heaviest component, C_{11+} .

Figure 4 summarizes the results of 20 simulations after 50% PV injection (PVI). Comparisons are made between 2D and 3D, DG and FV, and between IMPEC simulations versus IMPIC and AIM with 25, 50, and 100 times the CFL time-step size. Contours are shown for C_{11+} mole percentages of 15%, 50% and 95% throughout the domain in 2D and for a horizontal cross-section at $z = 5$ m for the 3D grid. For the 3D simulations, the composition profile is also plotted along a diagonal line from the injector to the producer.

Figure 4 shows that even for homogeneous domains, the time-step in AIM can be increased significantly while maintaining the same accuracy, whereas IMPIC shows considerably higher dispersion. Even for $100\times$ the CFL time-step, only 15% of the grid cells need to be updated implicitly, resulting in an overall CPU gain by a factor of 25. Almost the same speed-up is achieved by increasing the time-step 25-fold, in which case only 1% of the grid cells are updated implicitly (highlighted in red in Figure 4), illustrating that for homogeneous problems, channeling mostly occurs around wells.

All FV results have higher numerical dispersion, but the difference between AIM and IMPIC is less pronounced because the spatial error in FV is of the same order as the temporal error introduced by the larger implicit time-steps. FV-AIM simulations, though, are up to 57 times faster than FV-IMPEC. The 2D and 3D results show similar (lack of) numerical dispersion.

In short, even for homogeneous domains, AIM can achieve a factor 25–60 speed-up without sacrificing accuracy, and with low memory requirements.

4.2 Limitations of IMPEC for heterogenous and fractured domains

The same set-up is considered as in the previous example, but for three different porosity and permeability fields. In the first, a single grid cell at (200 m, 200 m) is given a 200 times lower porosity and 100 times higher permeability (for demonstrative purposes, in reality permeabilities and porosities are generally positively correlated). The second grid has a geostatistical distribution of correlated porosity and permeability values, and the third has two intersecting fractures with an aperture of 1 mm and permeability of 10^4 Darcy. The locations of the fractures are indicated, with exaggerated thickness, in Figure 5, which also shows DG simulation results for all three cases (in 2D).

The first test problem illustrates that a single element with a small PV can result in small time-steps for an entire IMPEC simulation, even though that element has no impact on the overall flow patterns. Nearly 50,000 time-steps of ~ 1.75 hrs were required to simulate 50% PVI by IMPEC. Both IMPIC and AIM easily allow 100 times larger time-steps in terms of numerical stability, and Figure 5 shows that AIM can do so without loss of accuracy, while IMPIC incurs higher numerical dispersion. This is because AIM only updates the wells and the low porosity grid cell implicitly, whereas IMPIC does so for the entire grid and leads to an unnecessarily dispersive spreading of the front. AIM is also more efficient and results in a speed-up by a factor 71, compared to 43 for IMPIC.

The second simulation makes the same point, but for geostatistically distributed rock properties that vary by orders of magnitude. Gravity is included in this example, and AIM and IMPIC simulations use 50 times larger time-steps than IMPEC. The conclusions in terms of computational efficiency and accuracy mimic those of the above example.

In the third simulation, flow is affected by two intersecting fractures in the middle of the domain. The fracture cells have both a small PV and experience the highest flow rates (due to high fracture permeability). Together, this results in exceedingly stringent CFL constraints. To make IMPEC simulations feasible at all, the cross-flow elements are given a width of 50 cm. In this case, an implicit transport update in the fractures (and wells) allows for 750 times larger time-steps than IMPEC, and again the numerical accuracy is not affected in the AIM simulation (while IMPIC shows higher numerical dispersion). Applications involving fractured reservoirs clearly benefit the most from the proposed AIM solution method.

4.3 Spatial and temporal adaptivity for a gravitational fingering problem

In the previous examples, the smallest CFL time-steps were determined by well locations and petrophysical properties. The associated grid cells that are updated implicitly in AIM remain (mostly) the same throughout a simulation and could be determined *a priori*. This example considers applications in which the highest flow velocities occur at the displacement front, which should therefore be updated implicitly for an efficient AIM scheme. Specifically, uniform CO₂ injection is considered from the top of a $(20 \times) 20 \times 100$ m³ vertical domain, discretized by elements of 50 cm in each direction. The porosity is 20%, and the permeability has a random lognormal distribution of ± 1.5 md around a mean of 50 md. FV simulations are performed on 2D and 3D grids with IMPEC, IMPIC, and AIM.

Because CO₂ is denser than the oil, the displacement front is gravitationally unstable. Fingers of CO₂-enriched oil propagate faster in the middle of the domain than near wells. The results are summarized in Figure 6. 2D and 3D implicit simulations use 10 and 50 times the CFL time-step size, respectively. All results show similar degrees of fingering and comparable numerical dispersion, but AIM shows significant increases in efficiency. In 2D, the simulation times for IMPEC, IMPIC, and AIM are 300, 45, and 25 secs, respectively. In 3D, the difference is even more significant at 76, 5, and 2 hrs.

This example shows how AIM improves the efficiency (35-fold) as compared to IMPEC, as well as the robustness of the switching logic. The CFL-based selection of implicit cells automatically tracks the front and results in a minimum number of implicit elements for a user-defined time-step size.

4.4 CO₂-brine transport in benchmark Egg Model reservoir

This example relates to solubility trapping of CO₂ during carbon sequestration in saline aquifers. Specifically, the transport of dissolved CO₂ is modeled as it is advected through an aquifer that has a fluvial depositional architecture. The grid and heterogeneous permeability distribution are taken from the benchmark Egg Model [Jansen *et al.*, 2014] in

which the porosity is a uniform 20% but permeabilities vary from 800 to 70,000 md, with high permeabilities organized in connected channels. To make the problem even more challenging, all permeabilities below 10 d are reduced by a factor 100, resulting in four orders of magnitude range in heterogeneity, and porosities are scaled linearly proportional to the permeability.

The grid is about $500 \times 500 \times 25 \text{ m}^3$ in size and has 18,553 unstructured elements (extruded from a Cartesian $60 \times 60 \times 7$ grid with inactive cells using the tools in the Matlab Reservoir Simulation Toolkit [Lie *et al.*, 2012]).

CO_2 -saturated brine (1.6 mol% dissolved CO_2) enters the domain at a constant rate of 1% PV/yr from the location indicated in Figure 7, while multiple wells placed around the domain perimeter achieve constant pressure outflow boundaries in x and y . The top and bottom of the formation are impermeable. The problem is simulated with the IMPEC, IMPIC, and AIM methods. The (adaptive)-implicit methods use 12 times larger time-steps than IMPEC. DG and FV transport updates are compared as well.

CO_2 dissolution increases the brine density by $\sim 1\%$, which is enough for CO_2 -saturated brine to gravitationally segregate to the bottom of the aquifer (Figure 7). CO_2 transport is dominated by the high permeability channels. The results show the same main conclusion as before: AIM achieves similar accuracy as IMPEC but at a lower computational cost. Only 5% of grid cells need to be update implicitly to achieve an order of magnitude larger time-steps (implicit cells are illustrated in the figure). DG-IMPIC does not increase the efficiency in this case, because the benefit of large time-steps is negated by the higher cost of each implicit update for the entire domain. The disadvantage of having to invert large matrices in DG-IMPIC (with 8 degrees-of-freedom for each grid cell) is overcome in DG-AIM when only a few grid cells have to be solved implicitly.

The additional computational cost of the higher-order DG-IMPEC and DG-AIM as compared to the lowest-order FV is only 20% on the same grid. Numerical dispersion of FV results in dispersive cross-flow between the high and low permeability regions and delays breakthrough of the front.

4.5 CO_2 transport in SPE 10 benchmark reservoir with 64 discrete fractures

The last two example combine all the features of the previous examples and apply those to industry-strength field-scale applications. The grid is taken from the SPE Tenth Comparative Solution Project [Christie and Blunt, 2001], which was constructed as a benchmark for upscaling techniques. Here the full resolution of the model is used for the bottom 5 layers, with $60 \times 220 \times 5$ grid cells for a $366 \times 670 \times 3 \text{ m}^3$ domain. These layers represent the Ness formation in the North Sea, which has high-permeability connected fluvial channels (consisting of sandstone) interspersed with low-permeability shales. The permeability distribution varies by 5 orders of magnitude. To further complicate the geometry and permeability field, 64 discrete connected and unconnected fractures are added with an aperture of 1 mm, fracture permeability of 10^6 md, and CFE width of 10 cm. The grid geometry is also modified by a sinusoidal variation of the height (by 20 m) in x and y to create a dome-like structure with non-orthogonal grid cells (Figure 8).

CO_2 -saturated brine enters from the top of the dome (indicated by a red arrow) at a constant rate of 5% PVI/yr. There are two constant pressure outflow boundaries (blue arrows) while the others are impermeable.

Figure 8 summarized the results for 5 simulations with different numerical methods. Physically, the CO_2 contours show three concurrent flow mechanisms: 1) pressure-driven flow from the injector to the outflow boundaries, 2) permeability channeling through both the fluvial sandstone pathways and connected fractures, and 3) down-dip gravity-driven flow in the transverse (x) direction due to the higher density of CO_2 -saturated brine.

In terms of numerical methods, IMPEC simulations are prohibitively expensive due to the large range in permeabilities and porosities. CFL constraints on the time-step are of the order of 10^{-4} days. Instead, FV-IMPIC and FV-AIM simulations are performed with $200\times$ the CFL time-steps, as well as DG-AIM with both $200\times$ and $1,500\times$ CFL, and DG-IMPIC with $1,000\times$ CFL. CO_2 molar fraction contour plots are shown at 10% and 20% PVI, and insets show the grid cells that are updated implicitly in AIM.

Because of the aforementioned CFL constraint on IMPEC simulations, even IMPIC and AIM simulations with 200–1,500 times larger steps still use reasonable average time-step sizes of 0.2–1.3 days. As a result, numerical dispersion is low and even FV results are close to the higher-order DG simulations. In fact, the results of all 5 simulations agree remarkably well. In terms of computation cost, the FV-IMPIC, FV-AIM simulations required 3.8 and 3.3 hrs, respectively, DG-AIM took 3.8 hrs with $1,500\times$ and 10 hrs with $200\times$ CFL, and DG-IMPIC cost 16.7 hrs. The difference between IMPIC and AIM is less than in some of the other examples because a large fraction of the grid cells contain fractures and 40% – 70% of cells have to be updated implicitly to allow $200\times$ – $1,500\times$ larger time-steps, respectively. The relatively high computation cost of DG-IMPIC in this example is due to the use of a direct solver and could be reduced by more efficient solvers, as well as by taking better advantage of the known sparsity patterns of the problem (see, e.g., *Natvig and Lie* [2008]; *Kwok and Tchelepi* [2007]).

4.6 Methane injection in SPE 10 benchmark reservoir with discrete fractures

As an energy-related generalization of the previous example, methane injection into a propane reservoir is modeled for the same fractured formation. Injection is uniform from one boundary at 5% PV/yr and production at a constant pressure from the opposite boundary (both locations are indicated in Figure 9). FV-IMPIC, FV-AIM, and DG-AIM results for the methane composition at 10% PVI are shown in Figure 9. Channeling of injected methane through the fluvial channels and connected fractures is even more profound in this example. Again, IMPIC and AIM simulations agree well, and the relative computational efficiencies are in line with the previous example.

5 Conclusions

The advantages of IMPEC and fully implicit schemes are well-known. The former is the most accurate, but becomes prohibitively CPU expensive for grids that have elements with small pore volumes and or high flow rates (e.g., fractures or coning around wells). The latter allows for large time-steps but exhibits high numerical dispersion and involves the solution of large matrix systems. Adaptive implicit methods (AIM) have been proposed to combine the benefits of each approach, while avoiding its pitfalls. In AIM, only the grid cells that incur strict CFL time-step constraints are updated implicitly while, ideally, most of the domain is modeled explicitly. This work applies AIM for the first time to higher-order FE methods for multicomponent compressible flow in (discrete) naturally fractured reservoirs. Numerical experiments demonstrate that this novel approach can achieve orders of magnitude higher computational efficiency than IMPEC, while maintaining similar accuracy. The last two examples show the efficiency and robustness of AIM for both hydrogeological and energy related applications in a field scale reservoir with dozens of fractures and 6 orders of magnitude range in rock properties. DG-AIM simulations were completed in only a few hours, while IMPEC would require nearly a month for the same problem. This sets the stage to model a wide range of challenging problems in hydrology and hydrocarbon reservoirs that would not be feasible with methods that require exceedingly small time-steps or suffer from high numerical dispersion.

Acknowledgements

The methodology and the data used for the numerical examples are described in the main text and cited references. This work was carried out without grant funding.

References

- Aarnes, J. E., T. Gimse, and K.-A. Lie (2007), An introduction to the numerics of flow in porous media using Matlab, in *Geometric modeling, numerical simulation, and optimization*, pp. 265–306, Springer.
- Abushaikh, A., M. Connolly, T. Garipov, F. Hamon, R. Iskhakov, S. Klevtsov, H. Pan, K. Terekhov, and P. Tomin (2009), General purpose research simulator, <https://supri-b.stanford.edu/research-areas/ad-gprs>.
- Acs, G., S. Doleschall, and E. Farkas (1985), General purpose compositional model, *SPE J.*, 25(4), 543–553.
- Bacon, D., M. White, and B. McGrail (2004), Subsurface transport over reactive multiphases (STORM): A parallel, coupled, nonisothermal multiphase flow, reactive transport, and porous medium alteration simulator, *Tech. rep.*, Pacific Northwest National Laboratory (PNNL), Richland, WA (US).
- Cainelli, O., A. Bellin, and M. Putti (2012), On the accuracy of classic numerical schemes for modeling flow in saturated heterogeneous formations, *Adv. Water Res.*, 47, 43–55.
- Cao, H., and K. Aziz (2002), Performance of IMPSAT and IMPSAT-AIM models in compositional simulation, in *SPE Annual Technical Conference and Exhibition*, doi:10.2118/77720-MS.
- Chang, Y.-B. (1990), Development and application of an equation of state compositional simulator, Ph.D. thesis, The University of Texas at Austin.
- Chavent, G., and J. Jaffre (1986), *Mathematical models and finite elements for reservoir simulation. Studies in mathematics and its applications.*, Elsevier, North-Holland.
- Chavent, G., and J. E. Roberts (1991), A unified physical presentation of mixed, mixed-hybrid finite-elements and standard finite-difference approximations for the determination of velocities in water-flow problems, *Adv. Water Res.*, 14(6), 329–348.
- Christensen, P., and K. Pedersen (2006), *Phase behavior of petroleum reservoir fluids*, CRC Press, Boca Raton, FL.
- Christie, M. A., and M. J. Blunt (2001), Tenth SPE comparative solution project: A comparison of upscaling techniques, *SPE Reserv. Eval. Eng.*, 4, 308–317, doi:10.2118/72469-PA.
- Clees, T., L. Ganzer, et al. (2010), An efficient algebraic multigrid solver strategy for AIM in oil-reservoir simulation, *SPE J.*, 15(03), 670–681.
- Coats, K. (2003), IMPES Stability: Selection of Stable Timesteps, *SPE J.*, 8(2), 181–187, doi:10.2118/84924-PA.
- Collins, D., L. Nghiem, Y. Li, and J. Grabonstotter (1992), An efficient approach to adaptive-implicit compositional simulation with an EOS, *SPE Res. Eng.*, 7(2), 259–264, doi:10.2118/15133-PA.
- Courant, R., K. Friedrichs, and H. Lewy (1928), Partial differential equations of mathematical physics, *Math. Annal.*, 100, 32–74.
- Forsyth, P., and P. Sammon (1986), Practical considerations for adaptive implicit methods in reservoir simulation, *J. Comput. Phys.*, 62(2), 265–281.
- Forsyth, P., P. Sammon, et al. (1986), Local mesh refinement and modeling of faults and pinchouts, *SPE Form. Eval.*, 1(03), 275–285.
- Fung, L. S., D. A. Collins, and L. X. Nghiem (1989), An adaptive-implicit switching criterion based on numerical stability analysis, *SPE Res. Eng.*, 4, 45–51.
- Grabonstetter, J., Y.-K. Li, D. Collins, and L. Nghiem (1991), Stability-based switching criterion for adaptive-implicit compositional reservoir simulation, in *SPE Symposium on Reservoir Simulation*, doi:10.2118/21225-MS.

- Hoteit, H. (2013), Modeling Diffusion and Gas-Oil Mass Transfer in Fractured Reservoirs, *J Petrol Sci Eng*, *105*, 1–17.
- Hoteit, H., and A. Firoozabadi (2005), Multicomponent fluid flow by discontinuous Galerkin and mixed methods in unfractured and fractured media, *Water Resour. Res.*, *41*(11), doi:10.1029/2005WR004339.
- Hoteit, H., and A. Firoozabadi (2006), Compositional modeling by the combined discontinuous Galerkin and mixed methods, *SPE J.*, *11*(1), 19–34, doi:10.2118/90276-PA.
- Hoteit, H., and A. Firoozabadi (2008a), An efficient numerical model for incompressible two-phase flow in fractured media, *Adv. Water Res.*, *31*(6), 891–905, doi: 10.1016/j.advwatres.2008.02.004.
- Hoteit, H., and A. Firoozabadi (2008b), Numerical modeling of two-phase flow in heterogeneous permeable media with different capillarity pressures, *Adv. Water Res.*, *31*(1), 56–73, doi:10.1016/j.advwatres.2007.06.006.
- Jansen, J. D., R. M. Fonseca, S. Kahrobaei, M. M. Siraj, G. M. Van Essen, and P. M. J. Van den Hof (2014), The Egg Model; a geological ensemble for reservoir simulation, *Geosci. Data J.*, *1*(2), 192–195, doi:10.1002/gdj3.21.
- Krogstad, S., K.-A. Lie, O. Møyner, H. M. Nilsen, X. Raynaud, and B. Skaflestad (2015), MRST-AD—an open-source framework for rapid prototyping and evaluation of reservoir simulation problems, in *SPE reservoir simulation symposium*, doi:10.2118/173317-MS.
- Kwok, F., and H. Tchelepi (2007), Potential-based reduced Newton algorithm for nonlinear multiphase flow in porous media, *J. Comput. Phys.*, *227*(1), 706–727.
- Li, Z., and A. Firoozabadi (2009), Cubic-plus-association equation of state for water-containing mixtures: Is cross association necessary, *AIChE J.*, *55*(7), 1803–1813.
- Lichtner, P. C., G. E. Hammond, C. Lu, S. Karra, G. Bisht, B. Andre, R. T. Mills, and J. Kumar (2013), PFLOTRAN Web page, <http://www.pflotran.org>.
- Lie, K.-A., S. Krogstad, I. S. Ligaarden, J. R. Natvig, H. M. Nilsen, and B. Skaflestad (2012), Open source MATLAB implementation of consistent discretisations on complex grids, *Comput. Geosci.*, *16*(2), 297–322, doi:10.1007/s10596-011-9244-4.
- Lu, P., J. S. Shaw, T. K. Eccles, I. D. Mishev, B. L. Beckner, et al. (2009), Experience with numerical stability, formulation, and parallel efficiency of adaptive implicit methods, in *SPE Reservoir Simulation Symposium*, doi:10.2118/118977-MS.
- Maes, J., A. Moncorgé, and H. Tchelepi (2013), Thermal adaptive implicit method: Time step selection, *J. Pet. Sci. Eng.*, *106*, 34–45.
- Mikysta, J., and A. Firoozabadi (2010), Implementation of higher-order methods for robust and efficient compositional simulation, *J. Comput. Phys.*, *229*, 2898–2913.
- Moncorgé, A., and H. A. Tchelepi (2009), Stability criteria for thermal adaptive implicit compositional flows, *SPE J.*, *14*(2), 311–322.
- Moortgat, J., and A. Firoozabadi (2013a), Three-phase compositional modeling with capillarity in heterogeneous and fractured media, *SPE J.*, *18*(6), 1150–1168, doi: 10.2118/159777-PA.
- Moortgat, J., and A. Firoozabadi (2013b), Higher-order compositional modeling of three-phase flow in 3D fractured porous media based on cross-flow equilibrium, *J. Comput. Phys.*, *250*, 425 – 445, doi:10.1016/j.jcp.2013.05.009.
- Moortgat, J., and A. Firoozabadi (2013c), Fickian diffusion in discrete-fractured media from chemical potential gradients and comparison to experiment, *Energ. Fuel*, *27*(10), 5793–5805, doi:10.1021/ef401141q.
- Moortgat, J., and A. Firoozabadi (2016a), Water coning, water and CO₂ injection in heavy oil fractured reservoirs, *SPE Res. Eval. Eng.*, doi:10.2118/183648-PA.
- Moortgat, J., and A. Firoozabadi (2016b), Mixed-hybrid and vertex-discontinuous-Galerkin finite element modeling of multiphase compositional flow on 3d unstructured grids, *J. Comput. Phys.*, *315*, 476–500, doi:10.1016/j.jcp.2016.03.054.
- Moortgat, J., Z. Li, and A. Firoozabadi (2012), Three-phase compositional modeling of CO₂ injection by higher-order finite element methods with CPA equation of state for aqueous phase, *Water Resour. Res.*, *48*, doi:10.1029/2011WR011736.

- Moortgat, J., M. A. Amooie, and M. R. Soltanian (2016), Implicit finite volume and discontinuous Galerkin methods for multicomponent flow in unstructured 3D fractured porous media, *Adv. Water Res.*, *96*, 389–404, doi:10.1016/j.advwatres.2016.08.007.
- Nasrabadi, H., J. Moortgat, and A. Firoozabadi (2016), New three-phase multicomponent compositional model for asphaltene precipitation during CO₂ injection using CPA-EOS, *Energ. Fuel*, *30*(4), 3306–3319, doi:10.1021/acs.energyfuels.5b02944.
- Natvig, J. R., and K.-A. Lie (2008), Fast computation of multiphase flow in porous media by implicit discontinuous Galerkin schemes with optimal ordering of elements, *J. Comput. Phys.*, *227*(24), 10,108–10,124.
- Peng, D.-Y., and D. B. Robinson (1976), A new two-constant equation of state, *Ind. Eng. Chem. Fundam.*, *15*(1), 59–64, doi:10.1021/i160057a011.
- Pruess, K. (2004), The TOUGH codes — a family of simulation tools for multiphase flow and transport processes in permeable media, *Vadose Zone J.*, *3*(3), 738–746.
- Russell, T., et al. (1989), Stability analysis and switching criteria for adaptive implicit methods based on the CFL condition, in *SPE Symposium on Reservoir Simulation*, doi:10.2118/18416-MS.
- Tan, T., et al. (1988), Implementation of an improved adaptive implicit method in a thermal compositional simulator, *SPE Res. Eng.*, *3*(04), 1–123.
- Thomas, G., and D. Thurnau (1983), Reservoir simulation using an adaptive implicit method, *SPE J.*, *23*(05), 759–768.
- Thomas, G., D. Thurnau, et al. (1982), The mathematical basis of the adaptive implicit method, in *SPE Reservoir Simulation Symposium*, doi:10.2118/10495-MS.
- Watts, J., and M. Rame (1999), An algebraic approach to the adaptive implicit method, in *SPE symposium on reservoir simulation*, pp. 221–230, doi:10.2118/51900-MS.
- Watts, J. W. (1986), A compositional formulation of the pressure and saturation equations, *SPE Reser. Eng.*, *1*(3), 243–252.
- Wheeler, J., and M. Wheeler (1990), IPARS technical manual, <http://csm.ices.utexas.edu/IparsWeb/iparsdocs.html>.
- White, M. D., D. H. Bacon, B. P. McGrail, D. J. Watson, S. K. White, and Z. Zhang (2012), STOMP subsurface transport over multiple phases: STOMP-CO₂ and STOMP-CO₂e guide, *Tech. rep.*, Pacific Northwest National Laboratory (PNNL), Richland, WA (US).
- Young, L., and T. Russell (1993), Implementation of an adaptive implicit method, in *SPE Symposium on Reservoir Simulation*, doi:10.2118/25245-MS.
- Zhou, Q., J. Bensabat, and J. Bear (2001), Accurate calculation of specific discharge in heterogeneous porous media, *Water resources research*, *37*(12), 3057–3069.
- Zhou, Y., H. A. Tchelepi, and B. T. Mallison (2011), Automatic differentiation framework for compositional simulation on unstructured grids with multi-point discretization schemes, in *SPE Reservoir Simulation Symposium*, doi:10.2118/141592-MS.
- Zidane, A., and A. Firoozabadi (2014), An efficient numerical model for multicomponent compressible flow in fractured porous media, *Adv. Water Res.*, *74*, 127–147.
- Zyvoloski, G. (2007), FEHM: A control volume finite element code for simulating subsurface multi-phase multi-fluid heat and mass transfer, *Los Alamos Unclassified Report LA-UR-07-3359*.

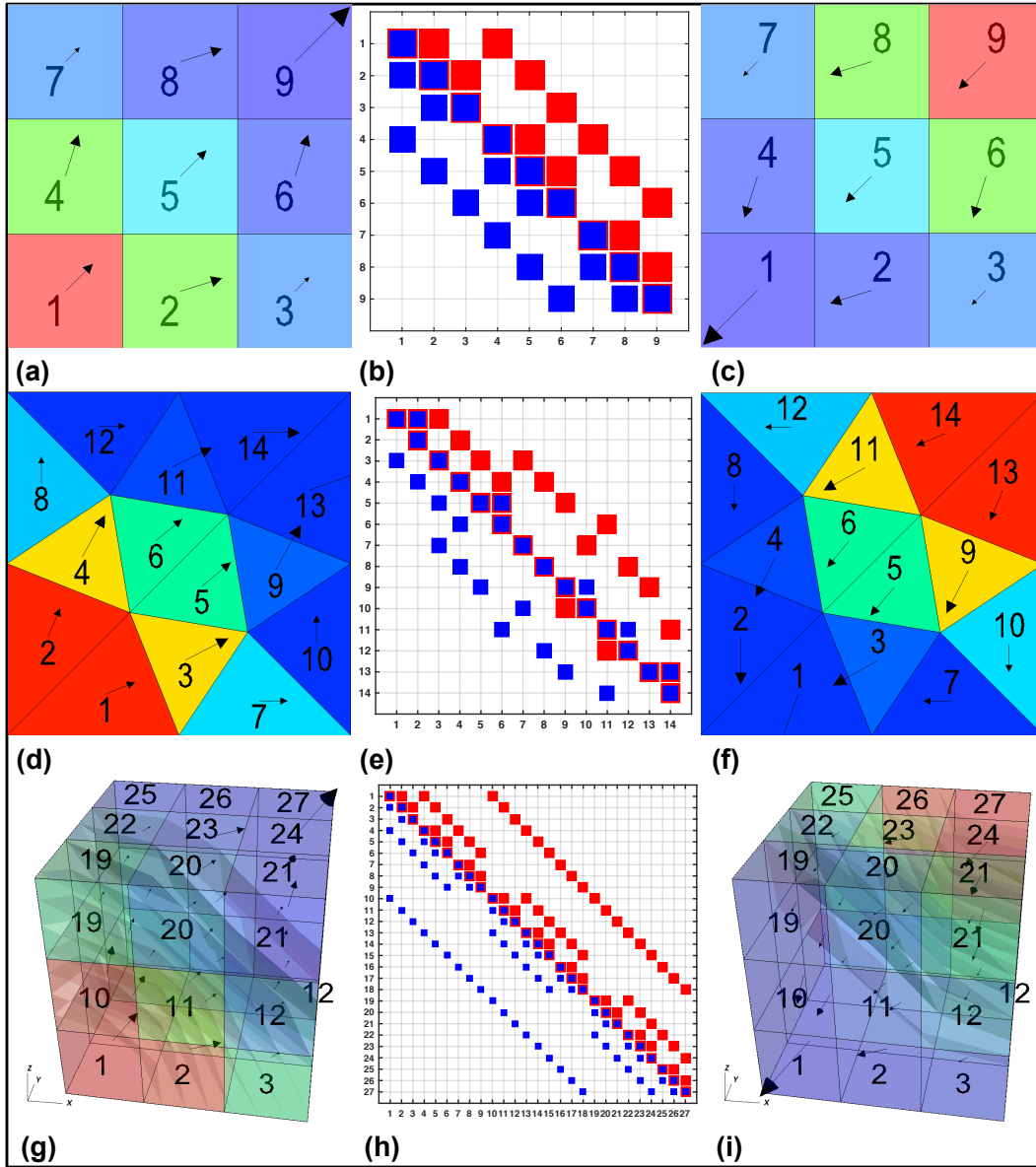


Figure 1. Sparsity patterns for FV transport updates on 3×3 quadrilateral (a)–(c), 14 element triangular (d)–(f), and $3 \times 3 \times 3$ hexahedral (g)–(i) grids. Fluid (composition shown in color at 50% PVI) is either injected from bottom-left(-front) and produced from top-right(-back) (a), (d), (g), or vice versa (c), (f), (i) (two injection cells are used for the triangular grid). The non-zero elements in matrix \mathbf{A}_{\pm} in Eq. 9 for the former case are shown in blue, and for the latter case in red, in the sparsity patterns (b), (e), (h) (note that there is overlap on the diagonal, and a few triangular elements). Arrows indicate the velocity field.

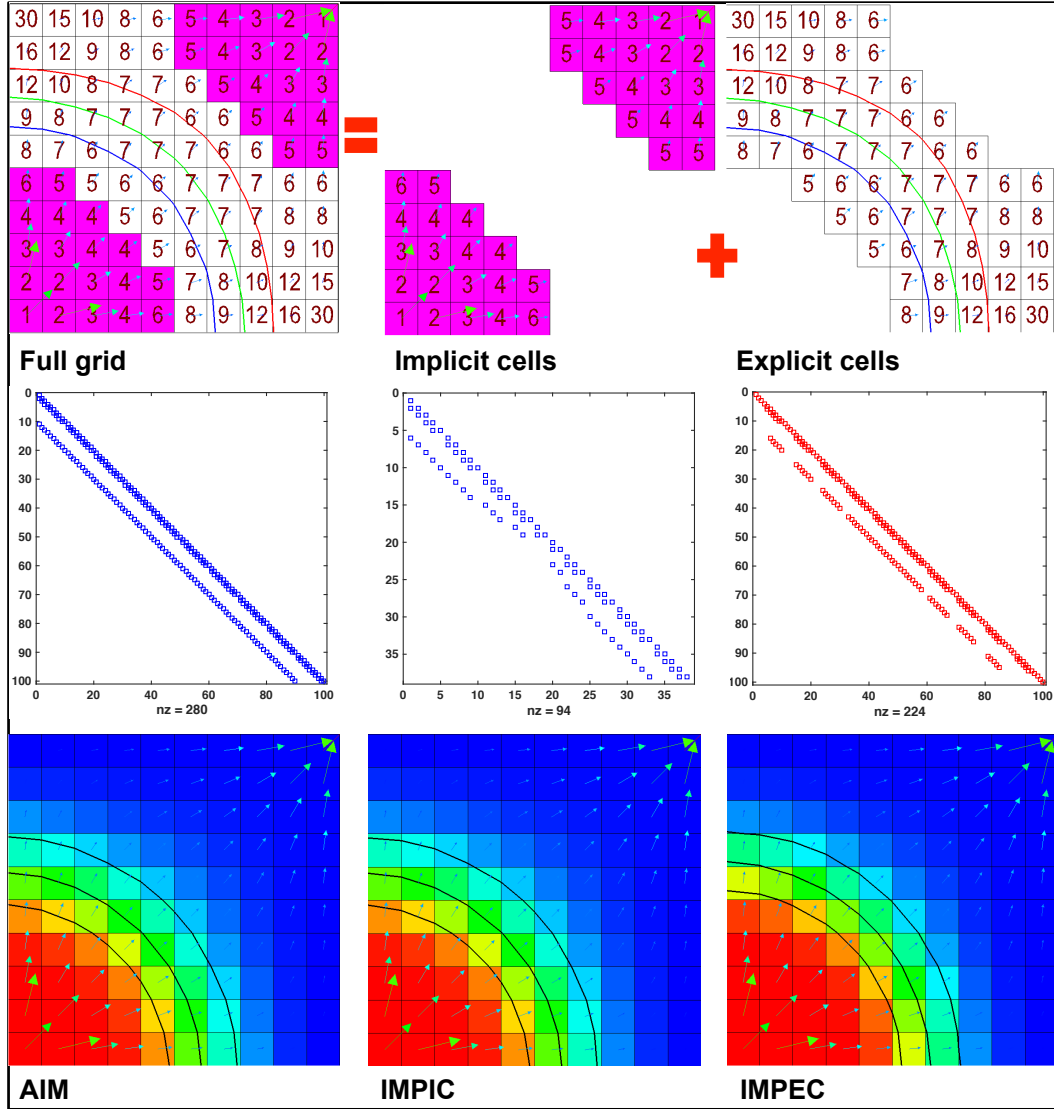


Figure 2. Splitting of a 10 × 10 quadrilateral grid in implicit (blue) and explicit (white) elements, based on a criteria of $\theta^{\text{switch}} = 4$ (Eq. 14 and smoothing discussed below). Contours show injection fluid after 40% PVI from bottom-left with production from top-right. Labels are for local CFL condition divided by the minimum CFL condition (Δt_{CFL}). Sparsity patterns are for a IMPEC or IMPIC simulation (280 non-zero matrix elements), for the AIM implicit update of the 38 elements (94 non-zeros), and for the 62 explicit elements (224 non-zeros). AIM, IMPIC, and IMPEC simulation results are shown in the bottom.

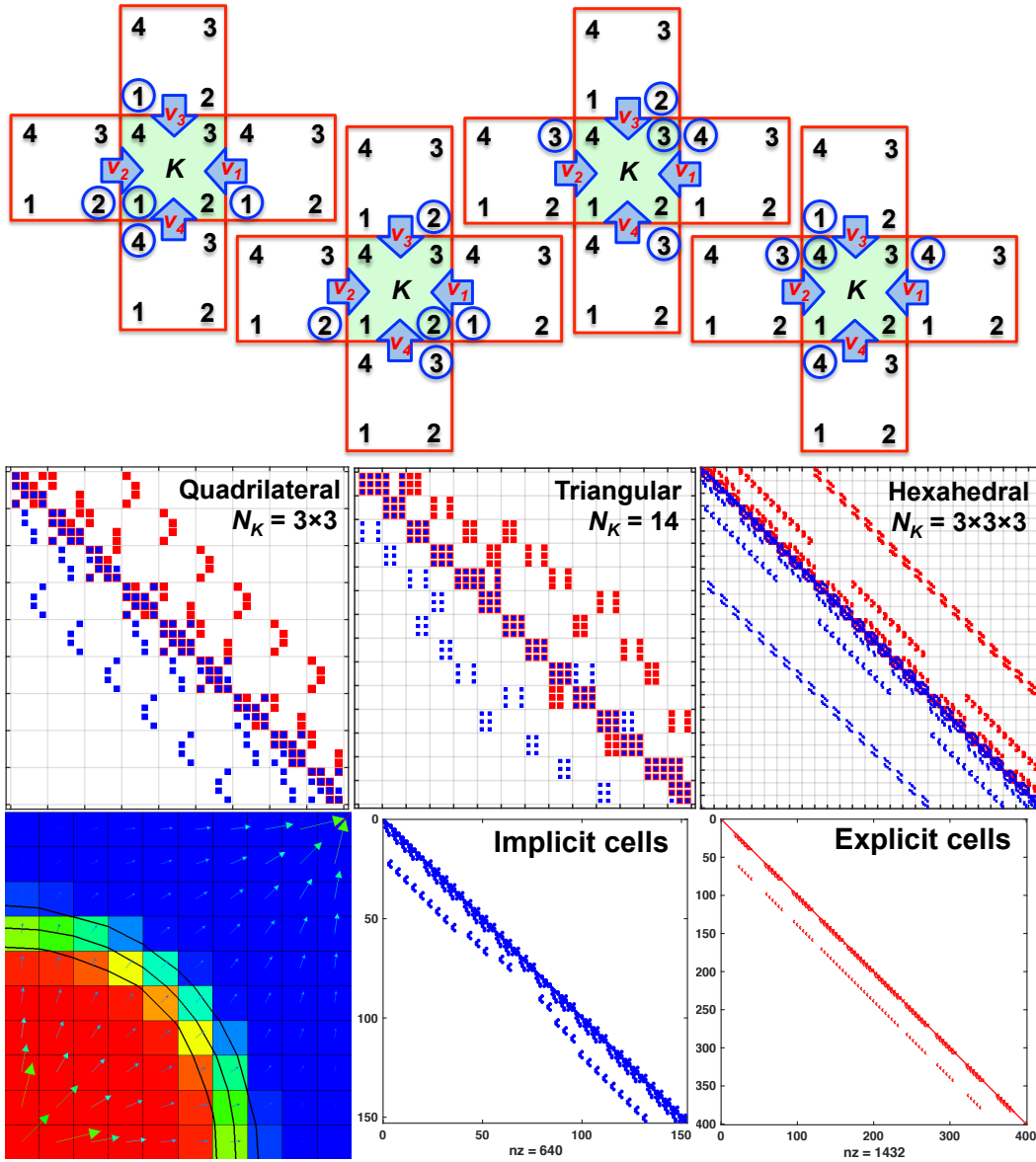


Figure 3. Numbering of nodes and face fluxes $v_{K,E}$ for a bilinear DG update on a quadrilateral grid. Each of the 4 top panels illustrates how the update of one nodal $c_{K,N}$ in the central element K depends on which nodal upwind values $\widetilde{c}_{K,E}$ in the 4 neighboring elements when $v_{K,E}$ is incoming. Sparsity patterns for the DG transport updates are shown for the same 3 grids as in Figure 1 (middle panels). DG-AIM results equivalent to Figure 2 are given in the bottom panels, as well as $\bar{\mathbf{A}}_+$ for the 4×38 implicit nodes (640 non-zeros), and $\bar{\mathbf{A}}_-$ for the 4×62 explicit nodes (1,432 non-zeros, out of 400^2).

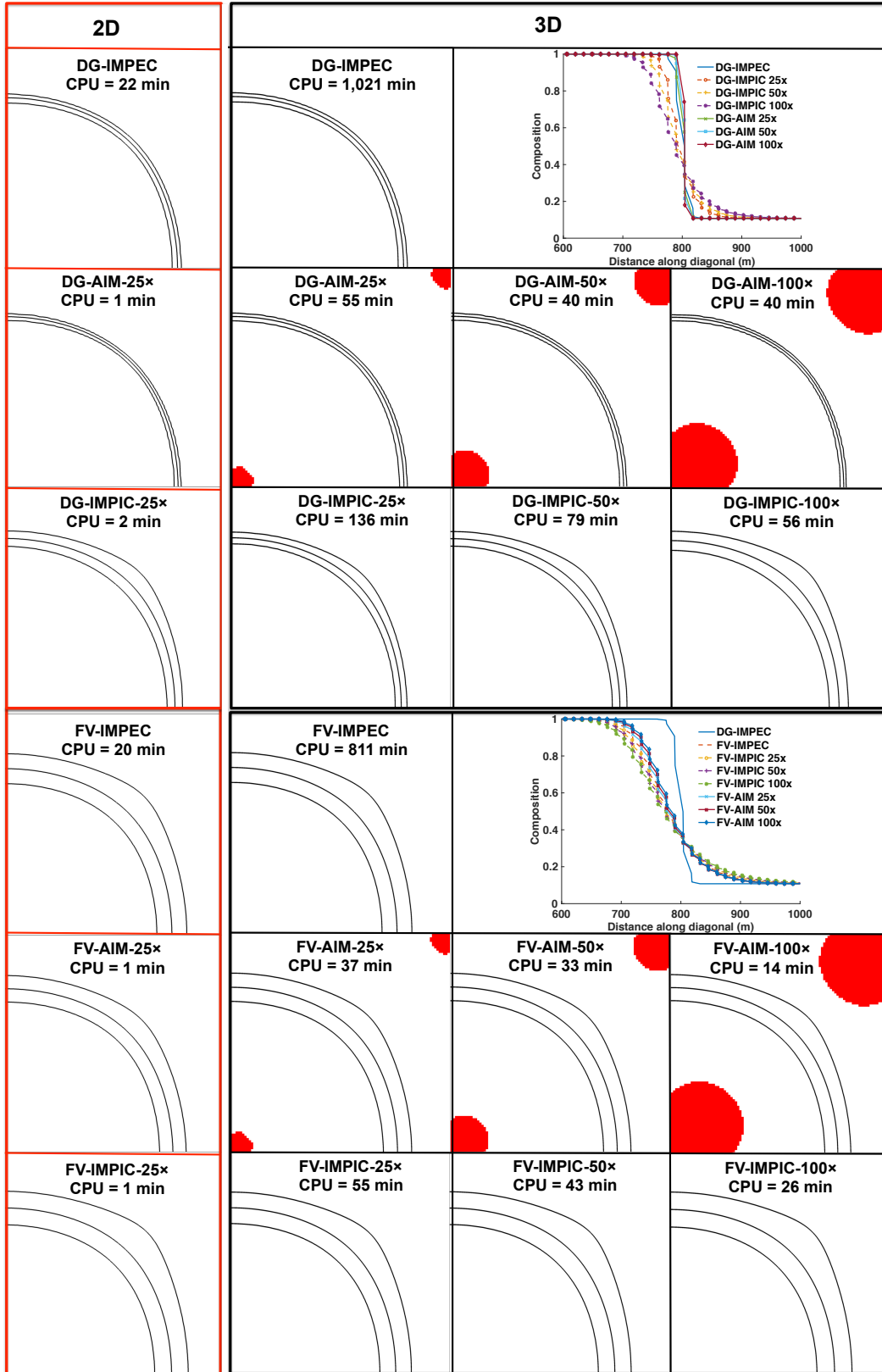


Figure 4. Example 1: C_{11+} mole percentage (contours for 15%, 50% and 95%) at 50% PVI, computed with different numerical methods on $1 \text{ km} \times 1 \text{ km}$ 2D and $1 \text{ km} \times 1 \text{ km} \times 100 \text{ m}$ 3D grids. The red grid cells are updated implicitly in the AIM simulations.

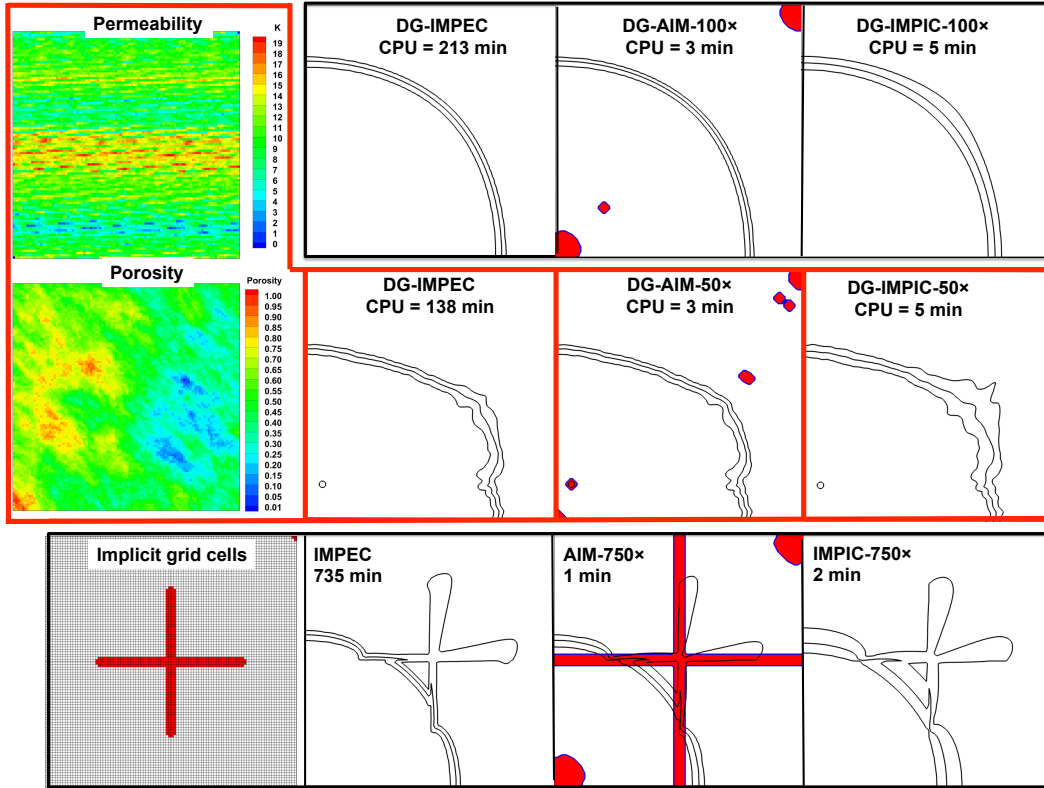


Figure 5. Example 2: C_{11+} mole percentage (contours for 15%, 50% and 95%), computed with different numerical methods on $1 \text{ km} \times 1 \text{ km}$ 2D grid. The red grid cells are updated implicitly in the AIM simulations. Top contour plots are for a grid with a single element that has a 200 times lower porosity (at 50% PVI). Middle panels are at 50% PVI for a geostatistical porosity and permeability distribution (shown in left panels) and includes gravity. Bottom panels are at 30% PVI for a grid with two intersecting fractures, as illustrated (thicker than actual grid cells) in the left panel.

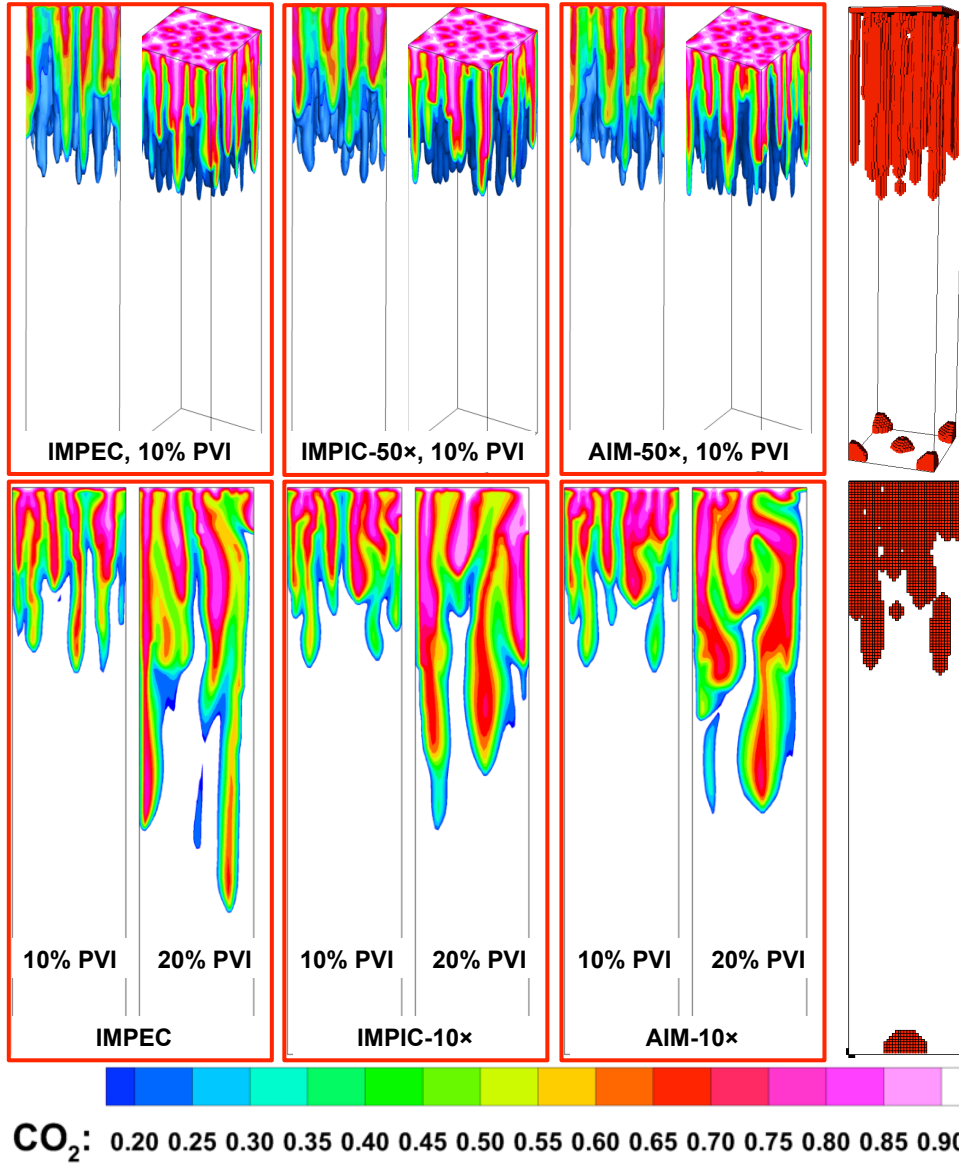


Figure 6. Example 3: CO₂ molar fraction in $(20 \times) 20 \times 100 \text{ m}^3$ 2D and 3D domains with 0.5 m grid sizes in each direction, computed with IMPEC, IMPIC, and AIM. CO₂ is uniformly injected from top and production is from bottom. Top panels show 3D results at 10% PVI, and on a cross-section at $y = 10 \text{ m}$. Bottom panels show 2D results at 10% and 20% PVI. Right-most panels show implicit grid cells in AIM.

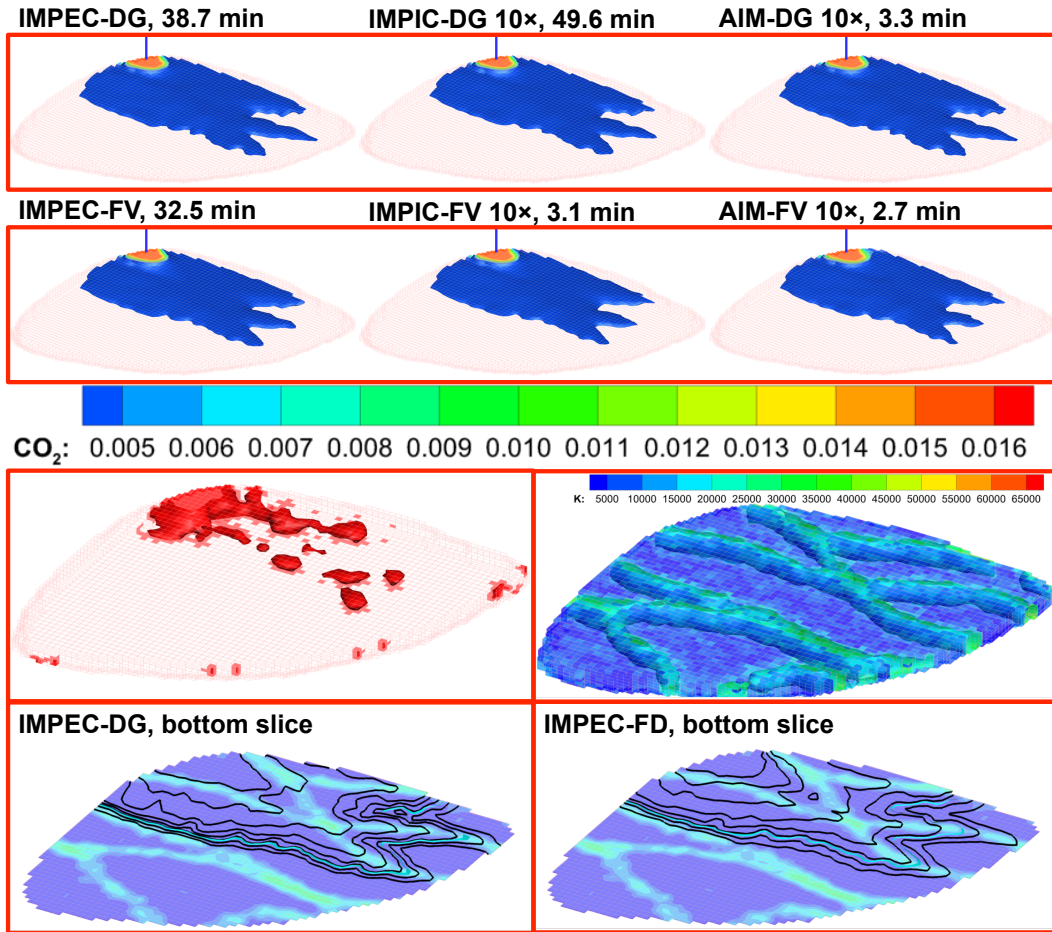


Figure 7. Example 4: Transport of CO₂ dissolved in brine through synthetic Egg Model reservoir. CO₂ molar fraction is shown for IMPEC, IMPIC and AIM for both DG (top row) and FV (second row) simulations, as well as a comparison between DG-IMPEC and FV-IMPEC CO₂ contours in the bottom layer (bottom panels). Insets show the grid cells that are updated implicitly in AIM (5% of grid cells) and the fluvial permeability field.

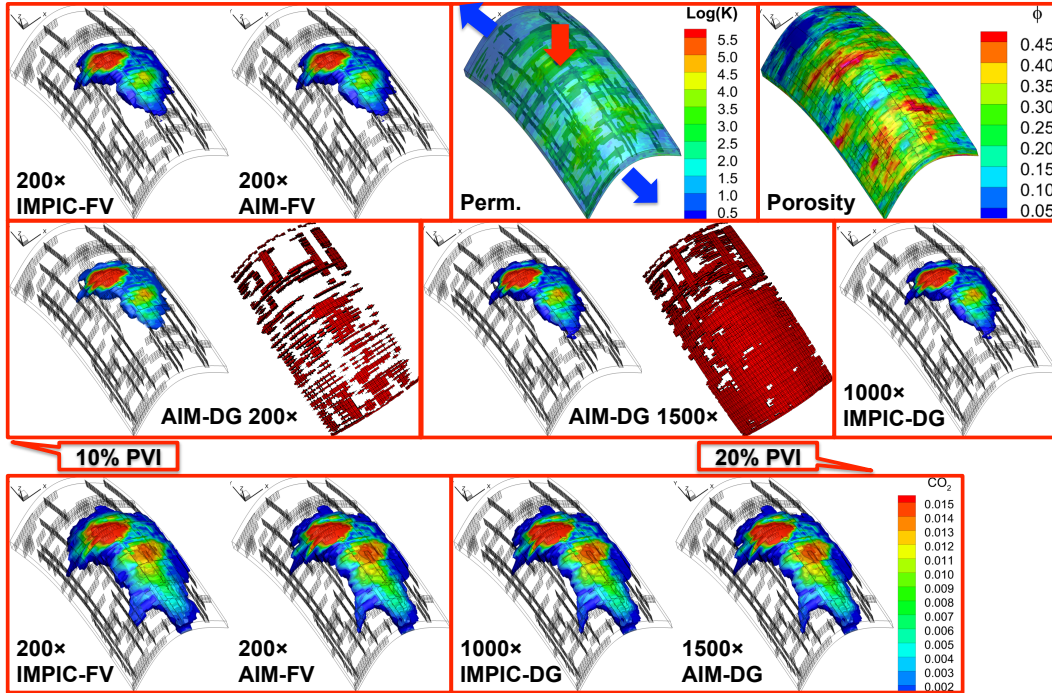


Figure 8. Example 5: CO₂ composition in heterogeneous and fractured reservoir. CO₂ enters top of dome structure (red arrow) at 5% PVI/yr and flows out constant-pressure boundaries (blue arrows). Top row shows permeability, porosity, and FV-IMPIC and FV-AIM results with 200× CFL at 15% PVI. DG-IMPIC with 1000× CFL, and DG-AIM with 200× and 1500× CFL are shown on the next row for the same time, with implicit grid cells illustrated in red in separate panels. Bottom row has similar results at 20% PVI.

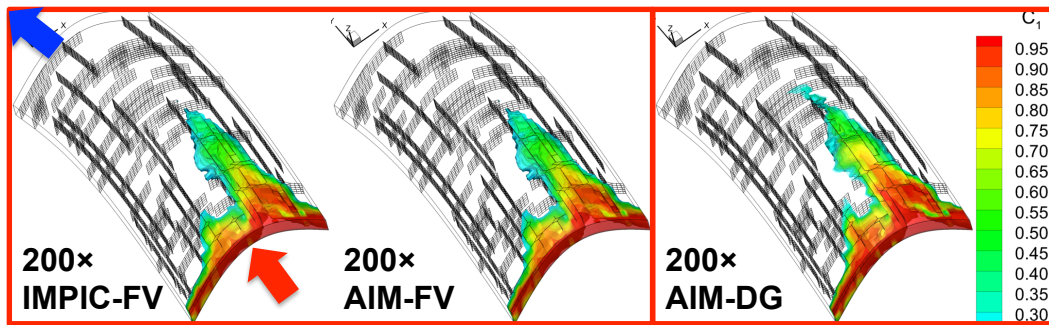


Figure 9. Example 6: Methane composition at 5% PV/yr for similar set-up as in Figure 8, but for uniform C₁ injection from one boundary (red arrow) with production from the opposite boundary (blue arrow).